AIAA JOURNAL
Vol. 49, No. 6, June 2011

Smart Double Panel for the Sound Radiation Control: Blended Velocity Feedback

Neven Alujević*
University of Southampton, Southampton, England SO17 1BJ, United Kingdom
Paolo Gardonio†
Università di Udine, 33100 Udine, Italy
and
Kenneth D. Frampton‡
University of Southampton, Southampton, England SO17 1BJ, United Kingdom

DOI: 10.2514/1.44284

In this paper an active damping method using blended velocity feedback for the reduction of sound transmission through a simplified aircraft double panel is considered. The double panel consists of a source and a radiating panel, which are coupled acoustically by the air in the cavity between them and structurally by four elastic mounts. The double panel is equipped with an array of nine voice-coil actuators that can react against the two panels. A velocity sensor is mounted at both panel junctions of each actuator. The outputs from the sensors on the source and radiating panels are weighted by factors α and $1-\alpha$, respectively. The two weighted signals are then subtracted and combined into the error signal fed back to the actuator via a constant amplification gain. The stability and performance of such a decentralized velocity feedback system are analyzed experimentally as a function of the weighting factor α. Reductions between −10 and −18 dB in the radiated sound power have been measured at low-frequency resonances of the double panel, depending on the weighting factor implemented.

Nomenclature

D	=	determinant of the return difference matrix
F_C	=	reactive actuator control force, N
$\mathbf{G}$	=	plant response matrix
$\mathbf{G_R}$	=	radiating panel component of the plant response matrix
$\mathbf{G_S}$	=	source panel component of the plant response matrix
g	=	feedback gain, Ns/m
$\mathbf{H}$	=	matrix of feedback gains, Ns/m
$\mathbf{I}$	=	identity matrix
j	=	$\sqrt{-1}$, imaginary unit
v_E	=	control error velocity, m/s
v_{rc}	=	velocity at a radiating panel control location, m/s
v_{sc}	=	velocity at a source panel control location, m/s
α	=	velocity weighting factor
α_{crit}	=	critical velocity weighting factor
δ_0	=	maximum negative real part of the open-loop sensor-actuator frequency response function, $\mathrm{ms^{-1}\,N^{-1}}$

I. Introduction

AIRCRAFT cabin noise is mainly caused by two principal sources: the power train (propeller or turbojet systems), and turbulent boundary-layer (TBL) pressure fields generated by the turbulent airflow over the skin of the aircraft [1,2]. Noise from internal sources, such as air-conditioning systems, may also be important [1,2]. Modern large passenger aircraft are equipped with turbojet engines in most cases. In these aircraft, an important source of cabin noise is due to jet noise, which is produced by the high-speed gas flow out of the engine exhaust. Normally jet noise dominates the interior noise field in low speed climb conditions [2]. However, jet noise can dominate the sound field in the rear passenger compartment even during cruise conditions if the engine nacelles are mounted close to the fuselage [2]. The frequency bands where jet noise contributes the most are those between 125 and 400 Hz [2]. Jet noise depends on the velocity of the exhaust jet, and high-bypass turbofans with a secondary low-velocity stream tend to be quieter. The jet power train can also contribute to the cabin noise at discrete frequencies. These frequencies are associated with the fan and compressor rotational speeds but the fan noise components are usually more important. This noise is transmitted into the cabin at frequencies that typically lie in the range of 75–200 Hz [2].

TBL noise has gained more importance since the introduction of commercial turbojet aircraft with high cruise speeds. The turbulent airflow over the fuselage surface is characterized by a fluctuating pressure that excites the fuselage skin. The boundary-layer pressure field is convected in the direction of the airflow. The convection speed is proportional to the aircraft speed such that at a certain cruise speeds hydrodynamic coincidence occurs [1–3]. In this case the phase of the boundary-layer-induced pressure matches the phase of the bending wave vibration of the fuselage skin. The consequent large vibration amplitudes of the fuselage skin result in large sound pressure levels in the aircraft cabin, particularly at mid and high frequencies, in the range between 400 and 2 kHz [2].

Both jet and TBL noise sources are transmitted to the cabin via the aircraft fuselage wall, which is normally composed by a frame structure with thin aluminum skin panels on the exterior, lightweight sandwich trim panels on the interior, and sound-absorbing blankets in the air gap between the skin and trim panels. The sound insulation properties of double panels are good at high frequencies, but they deteriorate as the frequency decreases [4]. In fact, at frequencies lower than the mass–air–mass resonance of a double panel, the transmitted sound is particularly high and its spectrum is characterized by well-separated resonances of low-order structural and acoustical modes of the double-panel system [4,5]. The sound transmission at these resonances can normally be reduced by adding

Received 10 March 2009; revision received 17 January 2011; accepted for publication 17 January 2011.

*Currently Research Fellow, Faculty of Electrical Engineering, Mechanical Engineering and Naval Architecture, University of Split, R. Boškovića, 21000 Split, Croatia.

†Professor, Dipartimento di Ingegneria Elettrica, Gestionale e Meccanica, Via delle Scienze 208.

‡Senior Lecturer, Institute of Sound and Vibration Research, University Road, Highfield.

damping materials to the vibrating partitions. However, the application of passive damping methods can result in too much added mass. For this reason, active damping methods have recently been proposed as a promising alternative to passive damping treatments [6].

Active damping can be applied to structures by embedding structural sensors and actuators that are then used to close negative velocity feedback loops [6–10]. This is often done in a decentralized manner, in order to ensure the robustness of the control system and to avoid the weight of the wiring, which is normally necessary when centralized control systems are used. Decentralized active damping systems are essentially multi-input/multi-output (MIMO) control systems whose stability is guaranteed if sensor-actuator pairs are dual and collocated [11–13].

Decentralized active damping in double panels can be applied via an array of reactive actuators mounted in the air cavity between the two panels [14–16]. The actuators can react against the two panels and apply control forces that aim to reduce relative velocities between the two actuator-panel junctions. The relative velocity error can be obtained by subtracting outputs of two velocity sensors that are mounted at the two footprints of each reactive actuator. The relative damping between source and the radiating panels can generate reductions of the resonant sound radiation up to the mass–air–mass resonance frequency. In particular, the radiated sound at the mass–air–mass resonant frequency can be efficiently reduced, since the governing mode is characterized by out of phase vibrations of the two panels [14].

Theoretical work has shown that the performance of relative velocity feedback control with a reactive actuator can be improved if the signals measured by the two velocity sensors are independently weighted before the subtraction [15]. In this way a combination of relative velocity and absolute velocity feedback is implemented with a reactive force actuator. This produces three effects: 1) a relative damping effect between the two panels, 2) a skyhook damping effect on the source or receiver panel, and 3) a flanking control action on the panel where no skyhook damping is produced. However, the stability of such a feedback loop depends on the proportion of the absolute velocity feedback with respect to the relative velocity feedback, i.e., it is function of the velocity weighting factor used. This is because the blended relative velocity sensor and reactive force actuator behave as dual and collocated only for a certain range of velocity weighting factors [15].

The primary contribution of this work is the experimental investigation of the stability and control performance properties of the smart double panel with a 3×3 array of blended (weighted) velocity feedback loops using reactive actuators. In particular it aims to show that with the use of appropriate velocity weighting factors the performance of the active control system can be improved in comparison to pure relative active damping approach.

This paper is organized in four sections. In Sec. II, the design of the smart double panel and the experimental procedures are described. In Sec. III the stability of individual feedback loops is analyzed using Nyquist criterion with respect to different velocity weighting factors used. Section IV is concerned with the performance of the active control system. The sound radiation measurement results are presented, which were performed in a large anechoic chamber. To generate a wider and more general range of test results, all acoustic tests were carried out on smart double panels with three different radiating panel materials (honeycomb, aluminum, and Perspex), and two different air cavity depths (deep and shallow). The control performance has been assessed with reference to a range of velocity weighting factors. The sound radiation measurements are presented in two frequency ranges: up to 500 Hz, in order to clearly show the low-frequency active damping effects; and up to 3.2 kHz, in order to present the broadband active and passive control effects. To assess the passive effects generated by the sensors and actuators, sound radiation measurements were taken on a plain double panel and when the double panel is equipped with open-loop or closed-loop control units.

II. Smart Double-Panel Design

In this section the design of the smart double panel experimental test rig is described. The source panel is built from an aluminum plate of 1 mm thickness. The radiating panel is built from a polymer plate of 3 mm thickness, constituted of a 2-mm-thick honeycomb core sandwiched between two face sheets of 0.5 mm thickness. As shown in Fig. 1 the radiating panel is attached to the source panel using four 30 mm long mounts located near the panel corners.

The space between the two panels is used to accommodate the array of nine sensor-actuator transducers. As can be seen in Fig. 1 the array is regular such that the control units are equidistantly spread over the surface of the two panels. Actuator coils are attached to the source panel and the permanent magnets are mounted onto the radiating panel. As shown schematically in Fig. 1 each coil and each magnet is equipped with an accelerometer sensor. The coils and magnets are carefully aligned such that no mechanical contact can occur between them during vibrations of the two panels. The detailed properties of the actuators and sensors can be found in [16].

The source panel is clamped between two thick aluminum frames, such that the free surfaces of the two panels equals 314×414 mm^2. The thickness of the bottom clamping frame is 25 mm, and the thickness of the top clamping frame is 40 mm. As a result the top clamping frame is slightly higher than the top surface of the radiating panel, such that the 30 mm deep air cavity is closed by the two panels and the inner side surfaces of the top clamping frame. Finally, as shown in Fig. 2, the whole assembly is mounted onto an open side of a Perspex box. Inside the box is there is a shaker that generates the primary disturbance at the source panel. The shaker pin is equipped with a force gauge whose output provides the primary excitation force. The box is made from 30-mm-thick plates of Perspex with the intention of minimizing the flanking transmission of sound generated inside the box. Therefore, the sound transmission through thin panels mounted on the box top is at least 10–20 dB higher than the flanking component radiated by the Perspex walls up to 5 kHz [9].

The control using the weighted velocity feedback is explained next. The error velocity is defined as

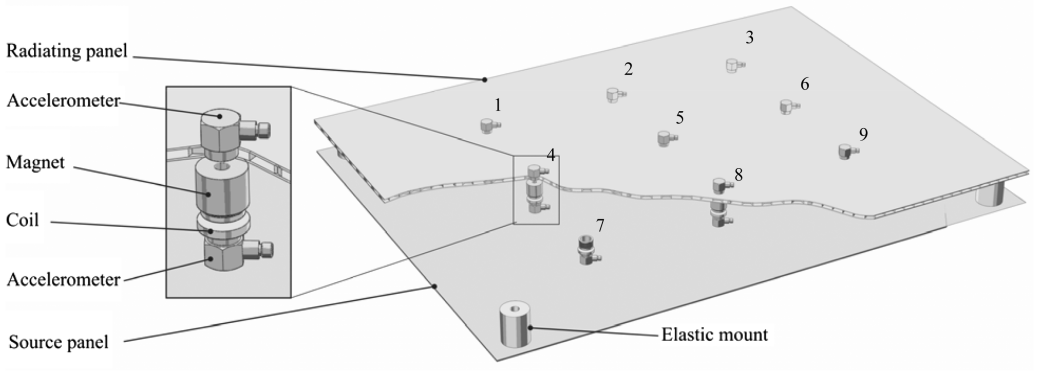

Fig. 1 Schematic representation of the prototype smart double panel with nine velocity feedback loops.

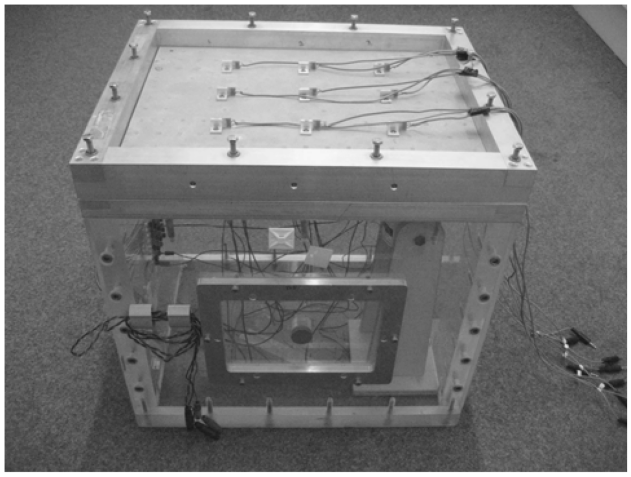

Fig. 2 Smart double panel and the clamping frame mounted on the Perspex box open side.

Fig. 3 Testing facility for the measurements of the sound radiation in the large anechoic chamber.

$$v_E = v_{\mathrm{rc}}(1-\alpha) - v_{\mathrm{sc}}\alpha \tag{1}$$

where v_{rc} is the velocity obtained by a time integration of the radiating accelerometer sensor output, v_{sc} is the velocity obtained by a time integration of the source accelerometer sensor output, and α is the velocity weighting factor.

In practice, when the feedback control loops are closed, the output signals of the source and radiating panel accelerometers are first independently amplified in order to implement the weighting of the two acceleration signals and then subtracted in order to obtain the error acceleration signal. The nine error acceleration signals are then fed to analogue integrators with identical amplification gains to provide the error velocity signals. If the two accelerometer outputs are amplified with equal gains, then a relative velocity between the coil and the magnet of each actuator unit is used as the error signal ($\alpha = 0.5$). Or alternatively, by varying source and radiating accelerometer gains, either the radiating or the source panel velocity can be emphasized such that error velocity signals with weighting factors between 0 and 1 are effectively obtained. Finally, the nine error signals are amplified by power amplifiers with equal amplification gains so as to drive the voice-coil actuators. To perform the entire signal processing task and to provide power for driving the actuators, a nine channel controller has been designed and fabricated [16].

As shown in Fig. 3, the testing rig is placed in a large anechoic chamber and excited by the shaker. Sound pressure measurements are made in nine positions around the box, according to the standard measurement procedure described by the ISO 3744. The radiated sound power is determined using the nine frequency response functions between the averaged sound pressures measured by the nine microphones and the shaker excitation force over the frequency ranges 0–500 Hz and 0–3.2 kHz.

The physical properties and the geometry of the prototype smart panel are summarized in Table 1. The smeared properties of the honeycomb radiating panel listed in Table 1 approximately correspond to the material properties of trim panels that are normally used for covering the interior walls in large passenger aircraft.

Hence the configuration with the honeycomb radiating panel has been chosen as the reference case studied in this paper. However, within the scope of the sound radiation analysis given in Sec. IV, two additional radiating panels were tested including a Perspex and an aluminum panel. The geometry and material properties of the Perspex and aluminum panels are listed in Table 2.

These materials are not normally used as interior panels in aircraft, but testing of these panels helps to generate a wider and more general range of test results. Furthermore, all configurations were also tested with a shallow cavity arrangement where the two panels are mounted at the distance of 13 mm rather than the original 30 mm distance. In the forthcoming text the 30 mm configuration is referred to as the deep cavity case, and the 13 mm cavity is referred to as the shallow cavity case.

III. Stability

The stability study presented in this section is organized in two parts. In the first part, the stability of each feedback loop is analyzed individually using the Nyquist criterion. Although this analysis is not

Table 1 Physical properties and the geometry of the prototype smart double panel

Parameter	Value
Dimension	414 × 314 mm
Source panel (aluminum)	
Density	2700 kg/m^3
Young's modulus	70 GPa
Poisson's ratio	0.33
Thickness	1.0 mm
Radiating panel (honeycomb)	
Density	255 kg/m^3
Young's modulus	15 GPa
Poisson's ratio	0.3
Thickness	3.0 mm
Mounts	
x position	21, 393 mm
y position	16, 298 mm
Stiffness	32,000 N/m
Cavity depth	30 mm
Box wall thickness	30 mm
Shaker	
x position	86.1 mm
y position	111.4 mm
Box inner dimension	414 × 314 × 400 mm

Table 2 Physical properties of Perspex and aluminum radiating panels

Parameter	Value
Dimension	414 × 314 mm
Perspex panel	
Density	1180 kg/m^3
Young's modulus	4 GPa
Poisson's ratio	0.3
Thickness	3.0 mm
Aluminum panel	
Density	2700 kg/m^3
Young's modulus	70
Poisson's ratio	0.33
Thickness	1.0 mm

sufficient to identify whether or not the full set of nine feedback loops is stable, it is particularly useful to establish necessary stability conditions of each control unit with reference to the weighting factor α. In the final part of this section, the stability of the whole set of feedback control loops is assessed with the generalized Nyquist criterion.

To perform the stability analysis of each feedback loop, the sensor-actuator open-loop frequency response functions for the nine feedback units of the smart panel were measured. A low-pass filter with 2500 Hz cutoff frequency was used and included in the open-loop sensor-actuator frequency response function (FRF) measurements. The upper frequency limit of the measurements was chosen to be 6400 Hz in order to include the resonant frequency of the microelectromechanical system accelerometers, which is at around 5.5 kHz.

Figure 4 shows Nyquist plots of nine sensor-actuator frequency response functions for all feedback units of the smart panel, numerated as in Fig. 1, when $\alpha = 0.5$, i.e., for relative velocity feedback control loops. Each Nyquist plot shows the majority of the circles in the right-hand side of the real–imaginary plane. These loops are due to the double-panel resonances. In each case a small circle appears in the left-hand side, which is due to the fundamental resonances of the two accelerometers [17]. Although there are differences between individual feedback units, in general they show similar behavior. The differences in the Nyquist plots of, for example, units 1, 3, 7, and 9, which should ideally be the same due to the symmetry of the test rig, indicate that actually there are asymmetries in the test rig and the sensor-actuator transducers, and/or nonhomogeneous material properties of the panels.

All plots in Fig. 4 indicate that although the relative velocity sensor and reactive force pair are theoretically dual and collocated (and therefore unconditionally stable), in practice, they are only conditionally stable. This is due to the fact that both the sensors and the actuator transducer have dynamic responses that, at a certain cut off frequency, disrupt the collocation and duality properties. In particular, it is the fundamental resonance of the accelerometers that causes the circles on the left-hand-side quadrants and thus disrupts the unconditional stability.

Figure 5 shows the amplitudes of the nine sensor-actuator open-loop frequency response functions. The solid lines are for the case with $\alpha = 0.5$, and the dashed lines are for the case with $\alpha = 0$.

Considering first the case with $\alpha = 0.5$, i.e., relative velocity feedback, the shapes of the nine open-loop sensor-actuator FRF amplitudes show well-separated low-frequency resonances that are due to the double-panel low-order modes. Typically, the amplitudes are maximum between 100 and 200 Hz and then roll off as the frequency increases. This effect can be attributed to the mass law that governs the response of the smart double panel at higher frequencies, and thus the shape of the open-loop sensor-actuator FRF amplitude. At 5.5 kHz there is a marked increase in the amplitude of each open-loop sensor-actuator FRF. This is due to the increased output of the accelerometers at their resonant frequency [17]. On the other hand, at very low frequencies (below 100 Hz), the resonance peaks due to double-panel low-order modes, are somewhat lower in amplitude. This indicates that the low-order mode passive damping may be relatively higher than predicted in the simulation study presented in [14,15]. The dashed lines in the nine plots show that the amplitudes of the nine sensor-actuator open-loop frequency response functions for the case with $\alpha = 0$, i.e., absolute velocity feedback, are quite similar to those for the case with $\alpha = 0.5$. The amplitudes of some low-frequency resonances are slightly different; in particular two resonance peaks are missing around 100 Hz.

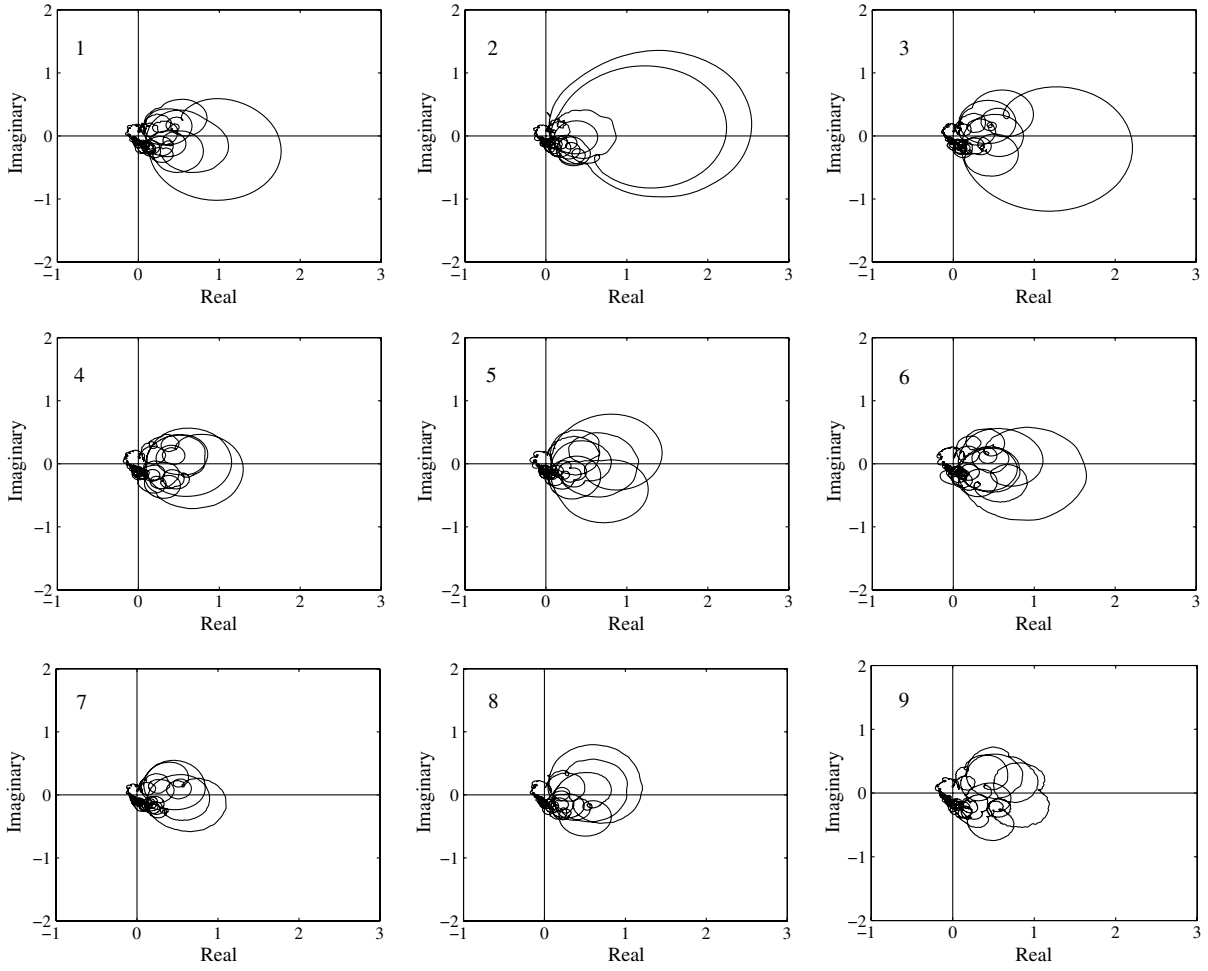

Fig. 4 Nyquist plots of nine open-loop sensor-actuator FRFs, with the velocity weighting factor $\alpha = 0.5$.

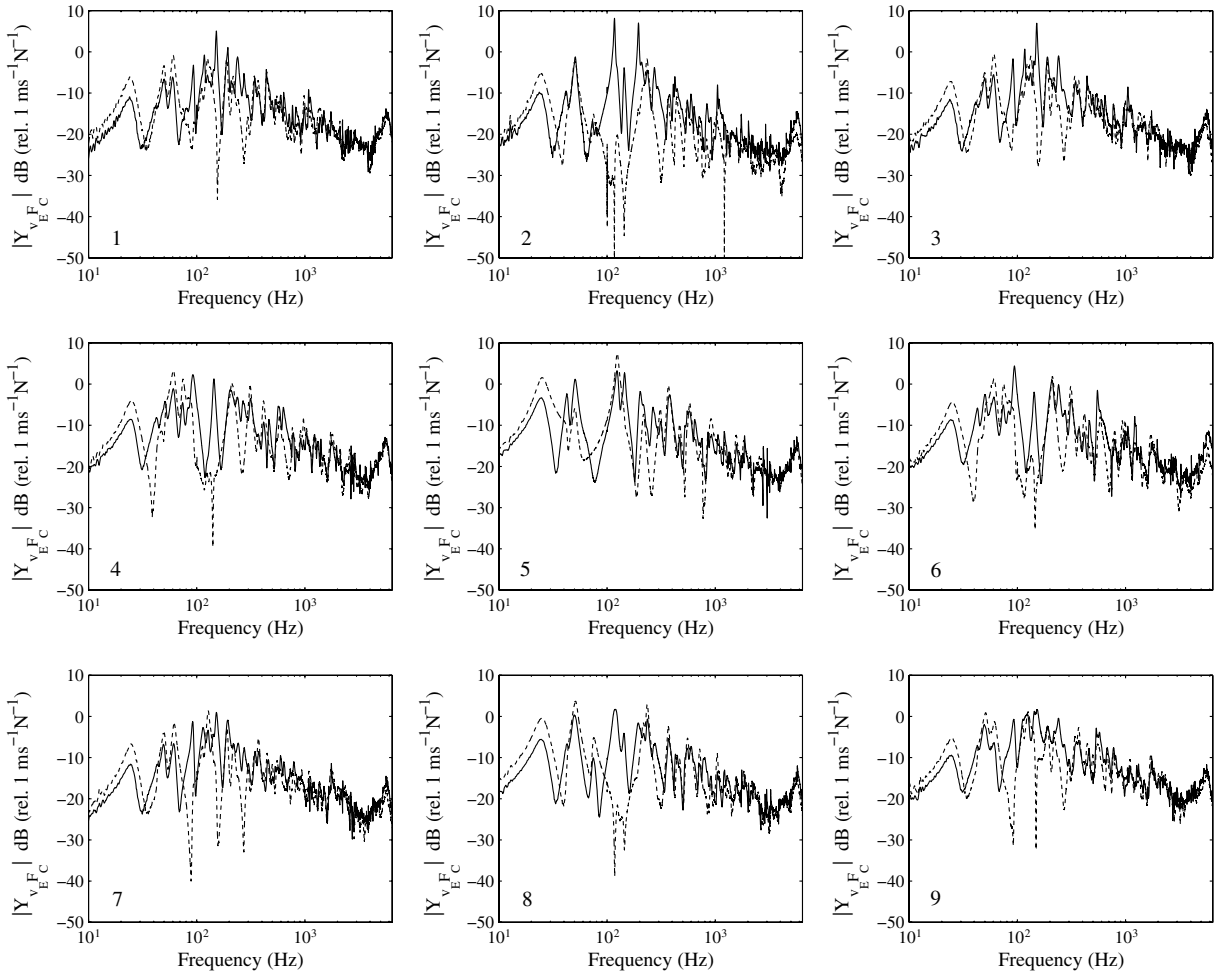

Fig. 5 Amplitude Bode plots of nine open-loop sensor-actuator FRFs, with $\alpha = 0.5$ (solid lines) and $\alpha = 0$ (dashed lines).

Figure 6 shows the nine open-loop sensor-actuator FRF phase angles. Again, the solid lines are for the case with $\alpha = 0.5$, and the dashed lines are for the case with $\alpha = 0$.

Considering the case with $\alpha = 0.5$, i.e., relative velocity feedback, the plots indicate that at low frequencies the open-loop sensor-actuator FRF phase angles are contained between -90 and 90 deg. However, at the resonant frequency of the accelerometers (5.5 kHz) the phase abruptly lags by 180 deg for all nine feedback units. Also, there is a gradual phase lag starting from 0 Hz to the higher frequencies due to low-pass filter effects. There are no 180 deg phase lags at lower frequencies, because the units feed the relative velocity back to the actuators (the velocity weighting factors equals $\alpha = 0.5$).

However, when the case for $\alpha = 0$ is considered, i.e., absolute velocity feedback, as demonstrated by the dashed lines in Fig. 6, the nine phase plots show that each of the nine feedback loops exhibits two successive lags of 180 deg. As found in the simulation studies presented in [15,16], the two lags occur at low frequencies between 80 and 100 Hz. This can lead to severe stability problems and the feedback gains can be further restricted because of the high amplitudes of the open-loop sensor-actuator FRFs at low frequencies. In addition, a negative real part of the open-loop sensor-actuator FRF at lower frequencies can cause spillover effects in the frequency range where control is aimed to reduce the response and the sound radiation of the double panel. To asses the impacts of these phase lags on the stability of the feedback loops, Nyquist plots of the nine open-loop sensor-actuator FRFs are analyzed for the case with $\alpha = 0$, i.e., absolute velocity feedback. As shown in Fig. 7, the Nyquist plots for those units that are close to the edges of the clamped source panel do not show increased amplitudes of the negative real parts of the open-loop sensor-actuator FRF in comparison to the relative velocity feedback case. But if unit number 5 is considered, which is located in the central area of the double panel, it is clear that the loop on the left-hand-side quadrants is considerably larger than in case with relative velocity feedback.

The differences between the units close to the panel boundary and the units in the central area of the panel can be explained by the fact that the impedance of the source panel at the actuator connecting point becomes larger as the connecting point gets closer to the clamped edges of the panel. Thus, the reactive forces of the outer control actuators will produce smaller source panel vibration amplitudes than the reactive forces of the inner control actuators. As a result the inner control units will produce large flanking excitations to the radiating panel, which occur with an intrinsic delay and thus disrupt the collocation and duality of the control force and velocity sensor on the radiating panel. This flanking phenomenon is not negligible for the inner control units and produces the stability problems highlighted by the Nyquist plots for the center control units shown in Fig. 7. This behavior of the open-loop sensor-actuator FRF and resulting stability issues are in agreement with the predictions using the theoretical model (see [15]).

To clearly demonstrate the effects of the velocity weighting factor on the available gain margin, two additional sets of measurements were performed. The first set involved measurements of nine radiating panel velocity signals with reference to nine corresponding reactive actuator forces:

$$\left(\frac{v_{\mathrm{rc}}}{F_C}(j\omega)\right)_{1,1}, \left(\frac{v_{\mathrm{rc}}}{F_C}(j\omega)\right)_{2,2}, \ldots, \left(\frac{v_{\mathrm{rc}}}{F_C}(j\omega)\right)_{9,9}$$

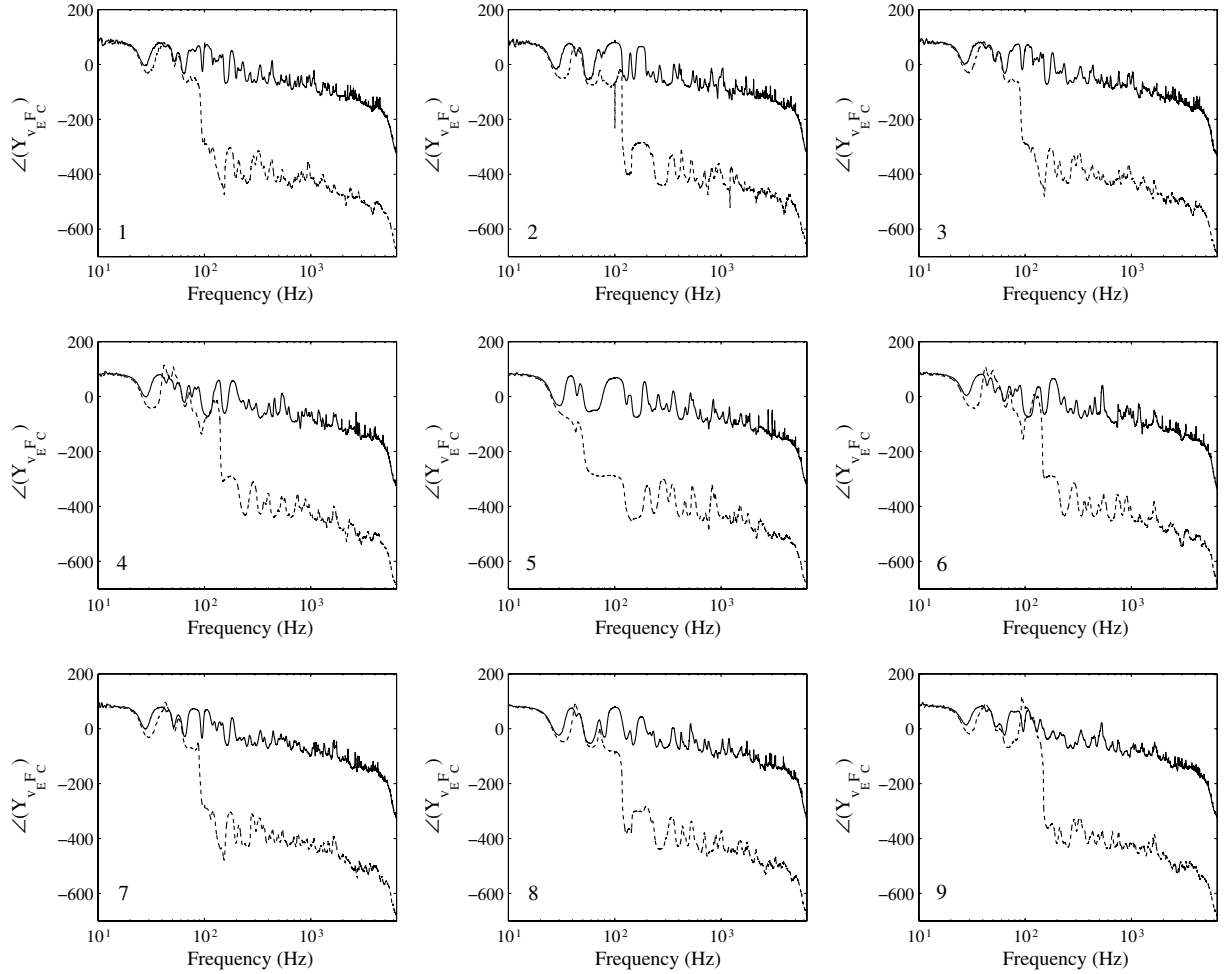

Fig. 6 Phase Bode plots of nine open-loop sensor-actuator FRFs, with $\alpha = 0.5$ (solid lines) and $\alpha = 0$ (dashed lines).

The second set involved a measurement of nine source panel velocity signals with reference to nine corresponding reactive actuator forces. The 18 FRFs were used for an offline reconstruction of the open-loop sensor-actuator FRFs with arbitrary velocity weighting factors according to the following expressions. If Eq. (1) is divided by the reactive actuator net force $F_C(j\omega)$ then it yields

$$\frac{v_E}{F_C}(j\omega) = \left[\frac{v_{\mathrm{rc}}}{F_C}(j\omega)\right](1-\alpha) - \left[\frac{v_{\mathrm{sc}}}{F_C}(j\omega)\right]\alpha \tag{2}$$

Therefore, if the frequency response functions $\frac{v_{\mathrm{rc}}}{F_C}(j\omega)$, and $\frac{v_{\mathrm{sc}}}{F_C}(j\omega)$ in Eq. (2) are known then it is possible to reconstruct offline the sensor-actuator open-loop frequency response functions $\frac{v_E}{F_C}(j\omega)$ for an arbitrary velocity weighting factor.

The nine open-loop sensor-actuator FRFs were reconstructed using the results of the two sets of measurements according to Eq. (2). Then the maximum negative real parts of the nine open-loop sensor-actuator FRFs were calculated and plotted against the velocity weighting factor α in Fig. 8. Each of the plots in Fig. 8 shows two types of results. The faint lines show the maximum negative real part of the open-loop sensor-actuator FRFs, indicated by δ_0 in the center plot of Fig. 7, plotted against the velocity factors ranging for zero to one, for the full frequency range 10–6400 Hz. Therefore, the available gain margins $1/\delta_0$, for each feedback unit can readily be calculated as a function of velocity weighting factor. However, it is not clear from such a representation whether the maximum negative real parts occur at low frequencies (due to the flanking actuation paths), or at high frequencies (due to the sensor fundamental resonance). For that reason the sensor-actuator frequency response functions were evaluated up to 2400 Hz, and the maximum negative real parts were determined for that frequency range, in order to capture the low-frequency behavior only. The corresponding results are plotted using solid lines in Fig. 8. The solid lines in the plots of Fig. 8 illustrate more clearly the stability effects of the low-frequency phase lags. As the velocity weighting factor α decreases from one to zero, the value of δ_0 is zero down to the critical velocity weighting factor, α_{crit} (see the center plot in Fig. 8). As the velocity weighting factors decrease further, δ_0 linearly decreases down to negative values. This effect is particularly visible at control unit number 5, because it is located at the center of the panel, where the source panel is more flexible and thus presents a smaller impedance to the actuator force.

The knee-shaped plots are very similar to those obtained theoretically in [15]. However, when comparing the theoretical results from [15] to the results obtained experimentally, the critical velocity weighting factor obtained experimentally (0.2) is lower than that obtained theoretically (0.375). This may be due to internal damping in each of the voice-coil actuators, which is generated by the viscous airflow through a small ring-shaped orifice between the actuator coil and magnet. The relative damping in the coil–magnet pairs effectively introduces an additional damper with a velocity weighting factor of $\alpha = 0.5$.

This results in an increased value of the true velocity weighting factor in comparison to the apparent velocity weighting factor. Considering now the remaining feedback units, the values of the critical velocity weighting factors are even lower. This may be attributed to the proximity of the source panel clamped edges, which tends to reduce α_{crit}. Such findings qualitatively agree with the predictions presented in [15].

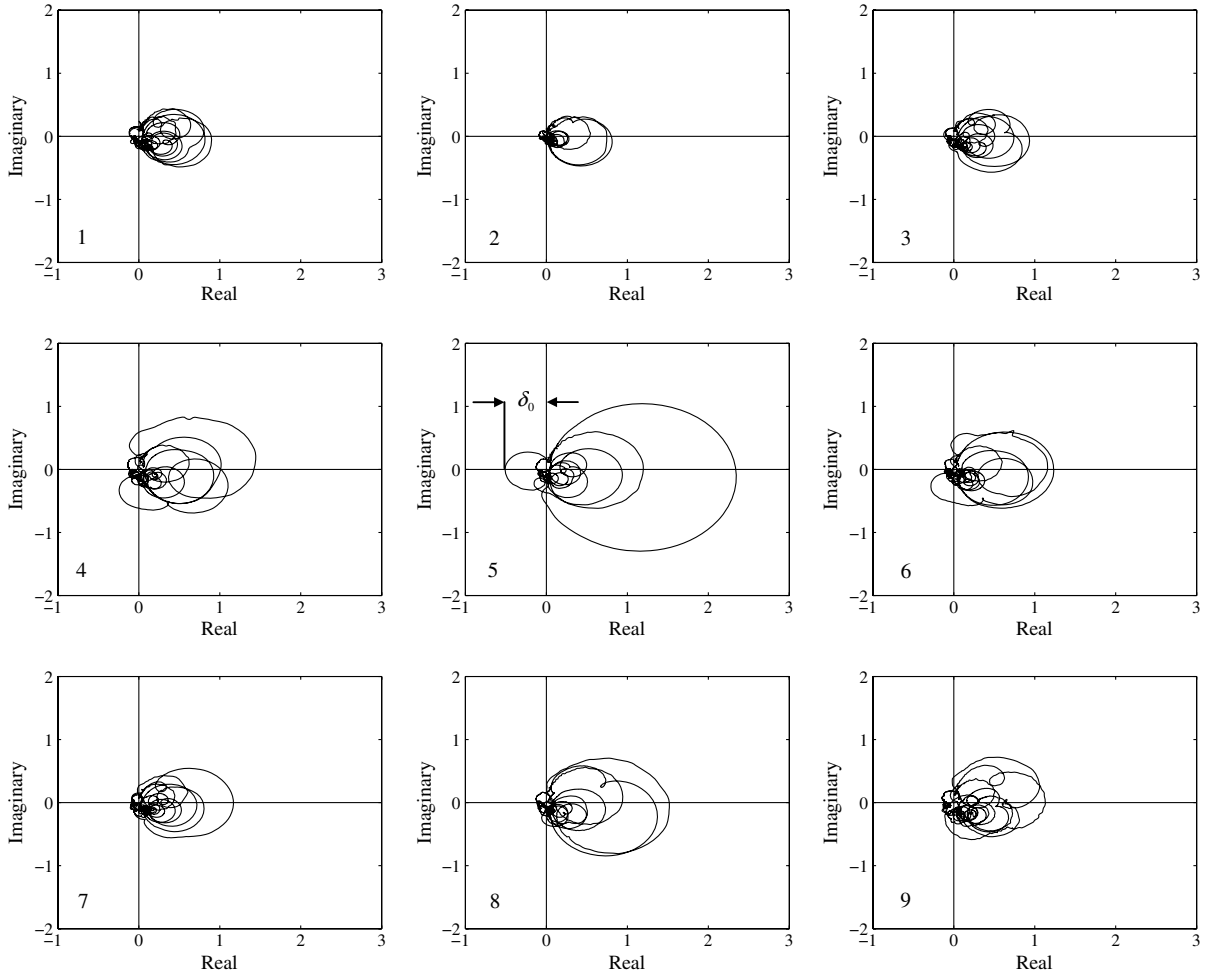

Fig. 7 Nyquist plots of nine open-loop sensor-actuator FRFs, with the velocity weighting factor $\alpha = 0$.

Although this analysis of individual loop stability demonstrates the physics that govern individual feedback-loop behavior, it cannot provide clear-cut conclusions concerning the stability of the nine channel system when the feedback loops are closed simultaneously. The generalized Nyquist stability criterion for MIMO systems should be used instead [18].

Assuming that the plant and the controller are individually stable, the generalized Nyquist criterion states that the closed-loop system is stable if and only if the locus of the determinant of the measured return difference matrix, $D(j\omega) = \det[\mathbf{I} + \mathbf{H}(j\omega)\mathbf{G}(j\omega)]$, does not encircle or pass through the origin, as the angular frequency ω varies between $-\infty$ and $+\infty$. Therefore, the full 9×9 matrix of the sensor-actuator frequency response functions $\mathbf{G}(j\omega)$ has to be determined as a function of the velocity weighting factor. To work out the matrix $\mathbf{G}(j\omega)$, two 9×9 matrices of the frequency response functions were first measured. The first matrix, $\mathbf{G_R}(j\omega)$, is a fully populated matrix of the frequency response functions between the nine radiating panel velocity sensors and the nine reactive actuators:

$$\mathbf{G_R}(j\omega) = \begin{bmatrix} \left(\frac{v_{rc}}{F_C}(j\omega)\right)_{1,1} & \left(\frac{v_{rc}}{F_C}(j\omega)\right)_{1,2} & \cdots & \left(\frac{v_{rc}}{F_C}(j\omega)\right)_{1,9} \\ \left(\frac{v_{rc}}{F_C}(j\omega)\right)_{2,1} & \left(\frac{v_{rc}}{F_C}(j\omega)\right)_{2,2} & \cdots & \left(\frac{v_{rc}(j\omega)}{F_C(j\omega)}\right)_{2,9} \\ \vdots & \vdots & \ddots & \vdots \\ \left(\frac{v_{rc}}{F_C}(j\omega)\right)_{9,1} & \left(\frac{v_{rc}}{F_C}(j\omega)\right)_{9,2} & \cdots & \left(\frac{v_{rc}}{F_C}(j\omega)\right)_{9,9} \end{bmatrix} \tag{3}$$

where $(v_{sc}/F_C(j\omega))_{i,j}$ is the frequency response function between the ith radiating panel sensor and the jth reactive actuator. The second matrix, $\mathbf{G_S}(j\omega)$, is a fully populated matrix of the frequency response functions between the nine source panel velocity sensors and the nine reactive actuator forces:

$$\mathbf{G_S}(j\omega) = \begin{bmatrix} \left(\frac{v_{sc}}{F_C}(j\omega)\right)_{1,1} & \left(\frac{v_{sc}}{F_C}(j\omega)\right)_{1,2} & \cdots & \left(\frac{v_{sc}}{F_C}(j\omega)\right)_{1,9} \\ \left(\frac{v_{sc}}{F_C}(j\omega)\right)_{2,1} & \left(\frac{v_{sc}}{F_C}(j\omega)\right)_{2,2} & \cdots & \left(\frac{v_{sc}}{F_C}(j\omega)\right)_{2,9} \\ \vdots & \vdots & \ddots & \vdots \\ \left(\frac{v_{sc}}{F_C}(j\omega)\right)_{9,1} & \left(\frac{v_{sc}}{F_C}(j\omega)\right)_{9,2} & \cdots & \left(\frac{v_{sc}}{F_C}(j\omega)\right)_{9,9} \end{bmatrix} \tag{4}$$

where $(v_{sc}/F_C(j\omega))_{i,j}$ is the frequency response function between the ith source panel sensor and the jth reactive actuator. The full 9×9 matrix of the sensor-actuator frequency response functions for a given velocity weighting factor can thus be calculated as

$$\mathbf{G}(j\omega) = (1-\alpha)\mathbf{G_R} - \alpha\mathbf{G_S} \tag{5}$$

The matrix $\mathbf{G}(j\omega)$ was calculated by using Eq. (5) for two example cases: $\alpha = 0$ and 0.5. The determinant $D(j\omega)$ was calculated using the gain matrix $\mathbf{H}(j\omega) = g \cdot \mathbf{I}$, where the value of g was chosen to be one. Figure 9 shows the locus of $D(j\omega)$ for the two cases.

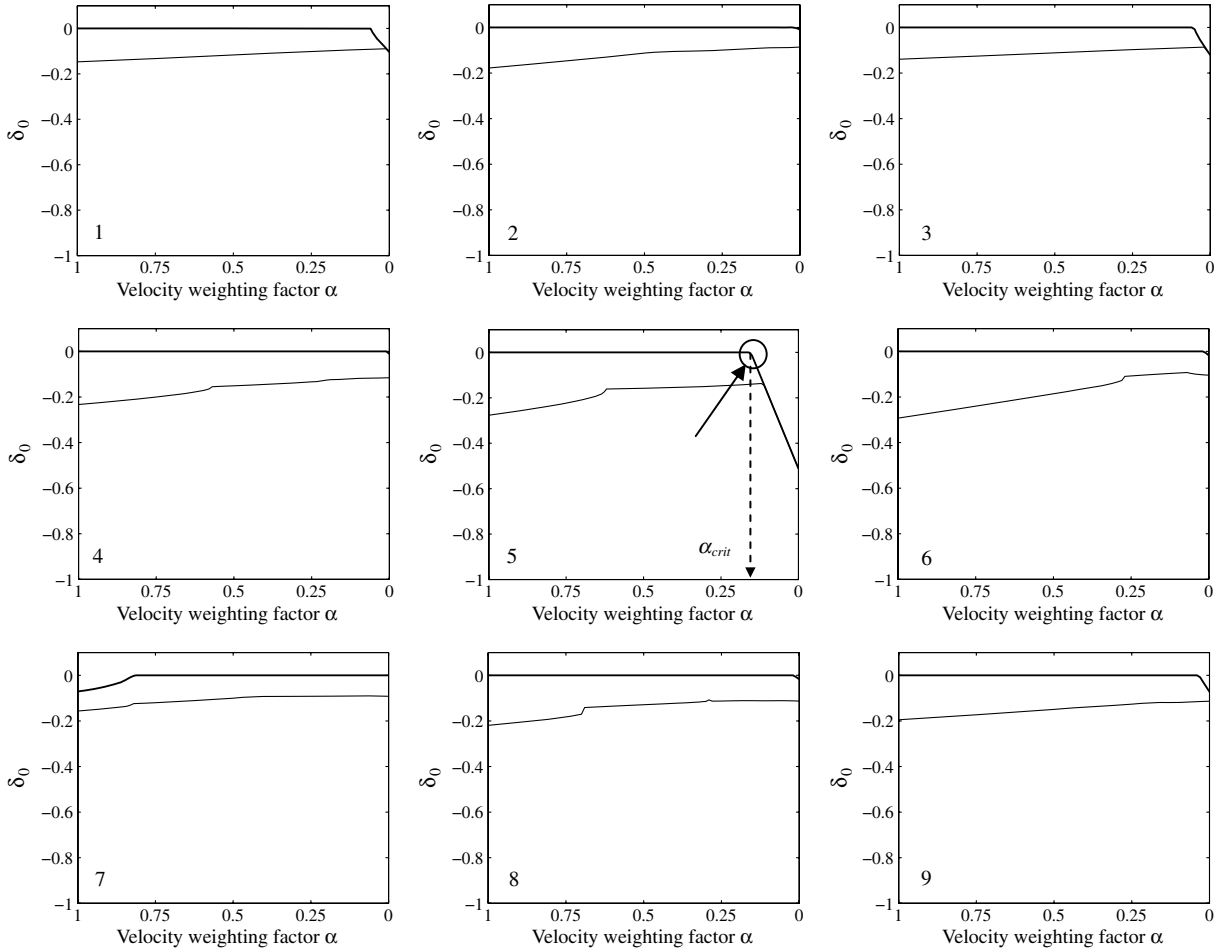

Fig. 8 Maximum negative real parts of the open-loop sensor-actuator FRFs, δ_0, plotted against the velocity weighting factor α, as calculated from experimental results, with frequency range 10–2400 Hz (thick lines) and with full frequency range 10–6400 Hz (thin lines).

The top plots of Fig. 9 are for the case with $\alpha = 0.5$, and the bottom plots are for the case with $\alpha = 0$. The right plots show zoomed areas around the origin of the left plots. The loci of the determinant $D(j\omega)$ in Fig. 9 are shown in different styles for three frequency ranges: 10–200 Hz as solid lines, 200–500 Hz as dashed lines, and 500 Hz–6.4 kHz as dotted lines. As shown in the top plots, the 3×3 MIMO system using $\alpha = 0.5$ is stable, since the locus of the return difference matrix determinant does not encircle the origin. However, as shown in the bottom plots, the 3×3 MIMO system using $\alpha = 0$ is unstable, because the locus of the return difference matrix determinant encircles the origin, as indicated by the arrow on the bottom right plot, even though the same feedback gain is used. Moreover, the frequency range of the encirclement is not around the accelerometer fundamental resonance. In contrast it occurs in the low-frequency range between 10 and 200 Hz, as shown by the solid lines in Fig. 9. This is probably due to the same flanking actuation paths that in case of asymmetrical weighting can cause the low-frequency phase lags observed within the individual feedback-loop stability analysis (see Fig. 6, dashed lines).

In conclusion, the stability analysis has highlighted that in order to avoid the low-frequency phase lags in the open-loop sensor-actuator FRFs and to increase the gain margin, the error signal has to be a blend of the source and radiating panel velocities rather than an absolute velocity of just one of the panels.

IV. Performance

A. Effects of Different Velocity Weighting Factors

In this section radiated sound power measurements are reported with respect to the control effects resulting from different velocity weighting factors in the feedback loops. Figure 10 shows the narrow band spectra of total radiated sound power for three deep cavity arrangements. The top plot in Fig. 10 shows the results with the honeycomb radiating panel, the middle plot is for the aluminum radiating panel, and the bottom plot is for the Perspex radiating panel.

The measured sound power spectra for three shallow cavity arrangements are plotted in Fig. 11, following the same layout as in Fig. 10.

The feedback gain was kept constant during the measurements. The preamplification factors of each of the source and radiating panel's sensors were set in order to achieve the desired velocity weighting factors. The faint lines designated as no control in Figs. 10 and 11 show the radiated sound power spectra when the control system is switched off. The remaining lines show the spectra when the active control system is switched on for different values of the velocity weighting factor. The grayscale lines are to show the results when the velocity weighting factor is increased from 0 to 1. The velocity weighting factor was varied in steps of 0.2.

The reference case with the deep cavity and honeycomb radiating panel is considered first. As shown by the solid line for $\alpha = 0$, the radiated sound power is increased at the lowest resonance (63 Hz) when active control is applied. This is because, according to the Nyquist criterion stability analysis given in Sec. III, the use of a velocity weighting factor $\alpha = 0$ results in the low-frequency phase lags of the nine sensor-actuator open-loop frequency response functions. Therefore, such a feedback configuration generates spillover effects due to the negative real parts of the nine sensor-actuator open-loop FRFs.

However, if the weighting factor is increased, as shown by the grayscale lines in the plots of Figs. 10 and 11, the sound radiation at the system lowest resonance decreases monotonically with increasing velocity weighting factor α. In particular, in comparison

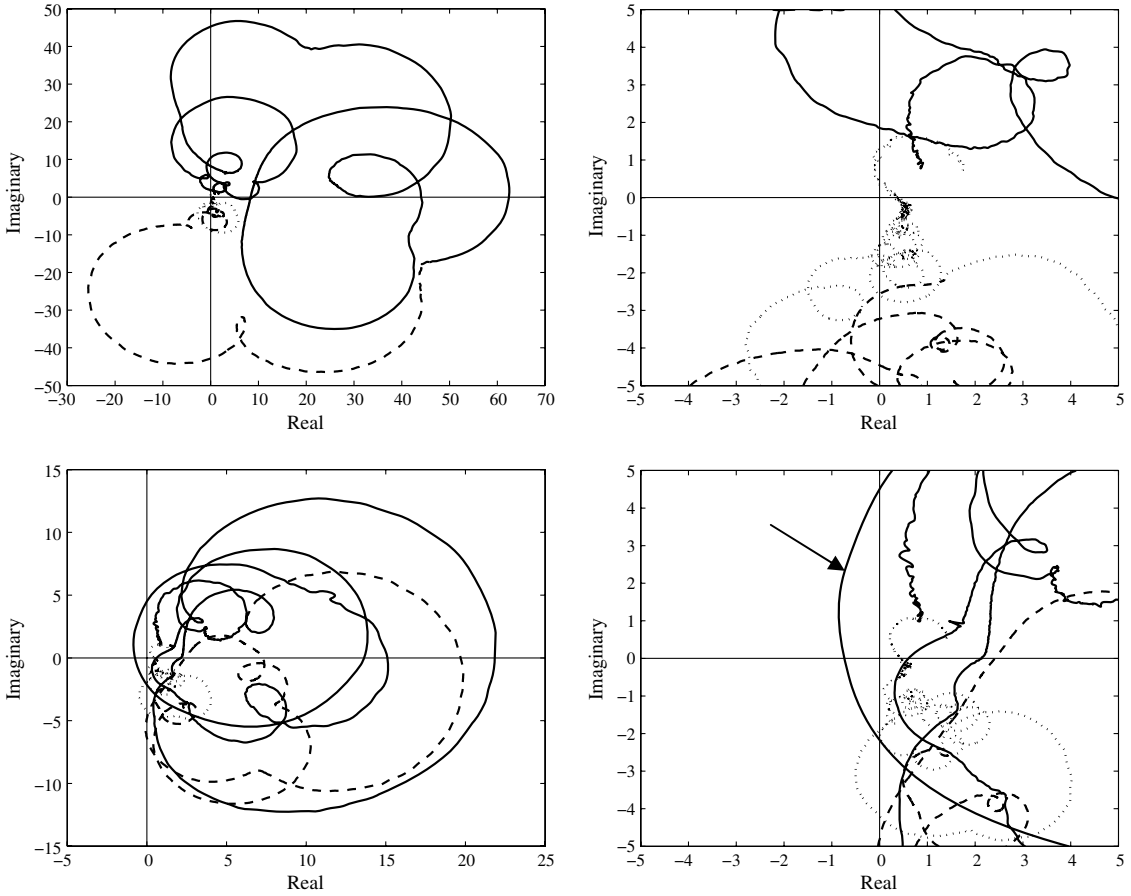

Fig. 9 Locus of $D(j\omega) = \det[\mathbf{I} + \mathbf{H}(j\omega)\mathbf{G}(j\omega)]$: case with $\alpha = 0.5$ (top) and case with $\alpha = 0$ (bottom); right images show zoomed areas around the origin of left images.

to the relative ($\alpha = 0.5$) velocity feedback performance, the use of $\alpha = 1$ generates an additional 8–10 dB reduction, for all tested double-panel configurations. The effect of the velocity weighting factor does not exhibit consistent trends at other frequencies. At frequencies close to the mass–air–mass resonance (~375 Hz), the use of $\alpha = 1$ still generates good performance, comparable to that of the relative velocity feedback. Although the active control system performs well in the analyzed low-frequency range, it is necessary to consider the effects of active control in a broader frequency band. For example, the theoretical performance study presented in [14] indicated that for very high feedback gains, new (lightly damped) resonances can occur at frequencies above the mass–air–mass resonance. For that reason the results of the sound power measurements are presented up to 3.2 kHz in the following subsection. Additionally, the effects of the added mass and damping by the sensor-actuator elements can be considerable, so this issue is also addressed in the next subsection.

B. Sensor-Actuator Passive Effects

In this section sound power measurements with and without active control were considered over a broader frequency band, from 30 Hz to 3.2 kHz. In particular, the spectra of the sound power radiated by the panels equipped with sensor and actuator transducers are compared with the spectra of a double panel with no transducers mounted. This type of analysis was performed because it was suspected that the passive effects generated by the sensors and actuators could have introduced passive damping as well as mass loading. Also, the purpose is to investigate possible high-frequency spillover effects produced by the control system due to the conditional stability of the feedback loops.

Figure 12 shows the sound power radiated by the smart panel plotted against frequency up to 3.2 kHz. The left-hand-side plot is with the deep cavity, and the right-hand-side plot is for the shallow cavity. The solid lines show the double-panel response without transducers, and the dashed lines are for the double panel equipped with the transducers but with the control system switched off. Therefore, the comparison of the solid and the dashed lines shows the passive effects of the control system transducers.

As can be seen in the figure, the passive effects are quite large as some of the low-frequency resonances are completely damped down when the transducers are mounted onto the panels. This is probably due to internal damping in each of the voice-coil actuators, which is generated by the viscous airflow through a small circular orifice between the actuator coil and magnet. This is because when the coil windings enter the gap between the two magnet poles, the air is pushed out of the magnet ring and vice versa. The viscous flow of the air through the small orifice causes the damping of the relative coil–magnet motion. In fact, due to the miniature actuator design and the requirements on the high magnetic flux in the orifice between the two poles of the magnet, the radial clearance between the coil and the magnet is as low as 0.25 mm. A more practical system might require a larger clearance in order to simplify actuator mounting and alignment. The larger clearance would result in smaller passive damping effects. The passive mass effects are visible in the mass controlled frequency range, above 500 Hz. Because of the added mass the dashed lines are shifted down relative to the solid lines at higher frequencies.

Active control performance is considered next. The feedback gain values and velocity weighting factors were selected to provide the best overall reductions of the radiated sound power in the broad frequency band up to 3.2 kHz. In the reference case this resulted in a velocity weighting factor of 0.4. As shown by the dotted lines in Fig. 12, the implementation of active control generates additional reductions between 5 and 15 dB at the resonant frequencies of the double-panel system.

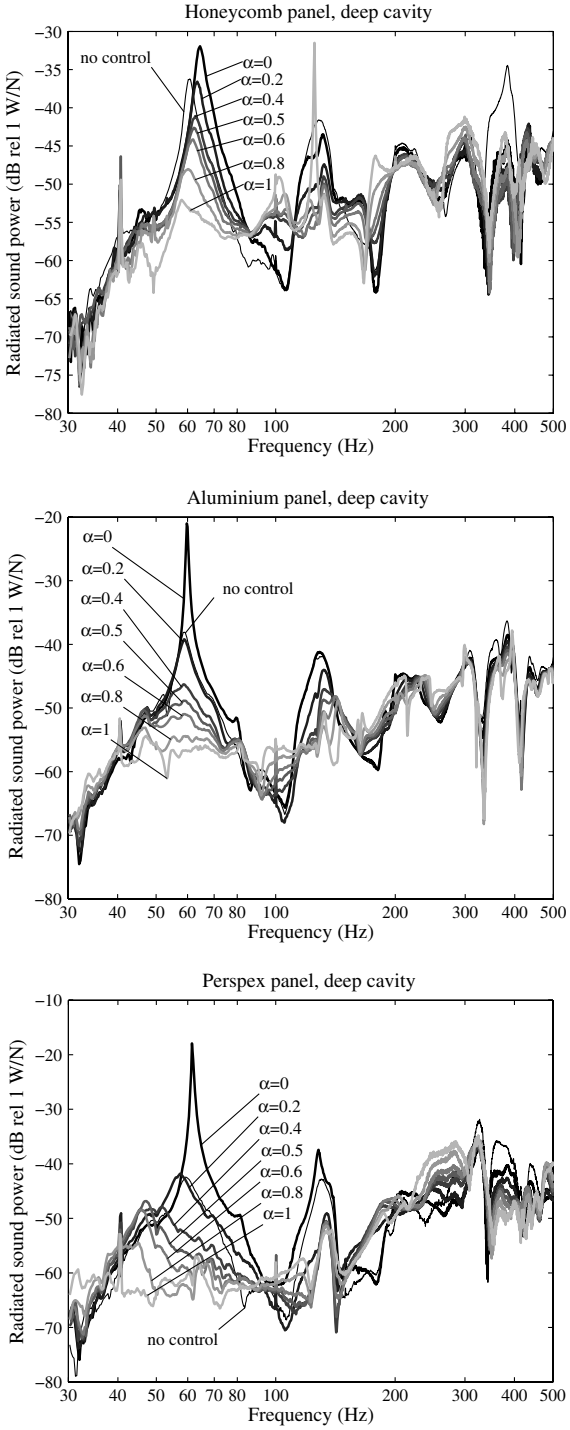

Fig. 10 Radiated sound power plotted against frequency in case when honeycomb (top), aluminum (center), and Perspex (bottom) radiating panels are used with the deep air cavity. Sound power spectra are shown for velocity weighting factors α increasing from 0 to 1.

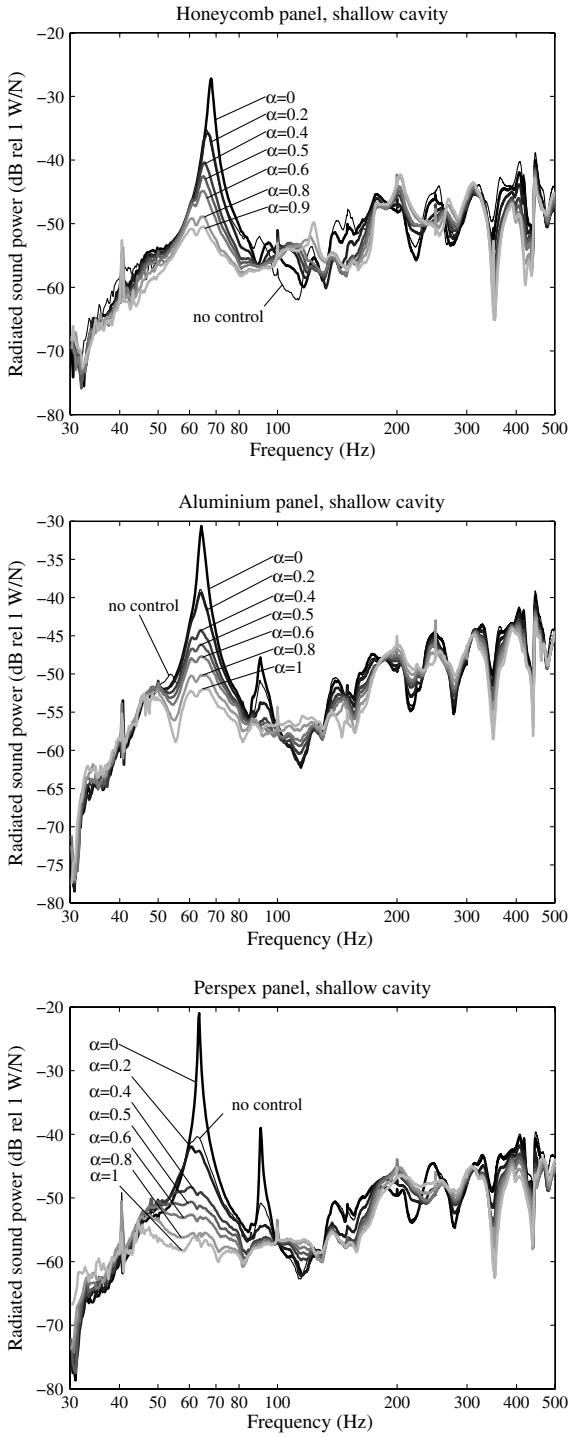

Fig. 11 Radiated sound power plotted against frequency in case when honeycomb (top), aluminum (center), and Perspex (bottom) radiating panels are used with the shallow air cavity. Sound power spectra are shown for velocity weighting factors, α, increasing from 0 to 1.

The right-hand-side plot in Fig. 12 show that similar qualitative passive and active effects are also obtained for the shallow cavity arrangement. The velocity weighting factor that provided the best broadband reductions was 0.3 for the honeycomb radiating panel with the shallow cavity.

To complete the study of the broadband active and passive effects, the same type of measurements (with/without transducers and with with/without active control) of the radiated sound power were also performed for the double panels with the aluminum and Perspex radiating panels, with deep and shallow air cavities between source and radiating panels. Figure 13 shows the radiated sound power spectra for Perspex radiating panel with deep cavity (left-hand-side plot), and Perspex radiating panel with shallow cavity (right-hand-side plot).

Figure 14 shows the radiated sound power spectra for the aluminum radiating panel with deep cavity (left-hand-side plot), and the aluminum radiating panel with shallow cavity (right-hand-side plot).

As shown in Figs. 13 and 14 large passive effects are also generated by the coil/magnet pairs in these cases. In addition, active control generates additional damping of the low-order vibratory modes, such that the radiated sound power is reduced by 8–10 dB at the low-order mode resonances.

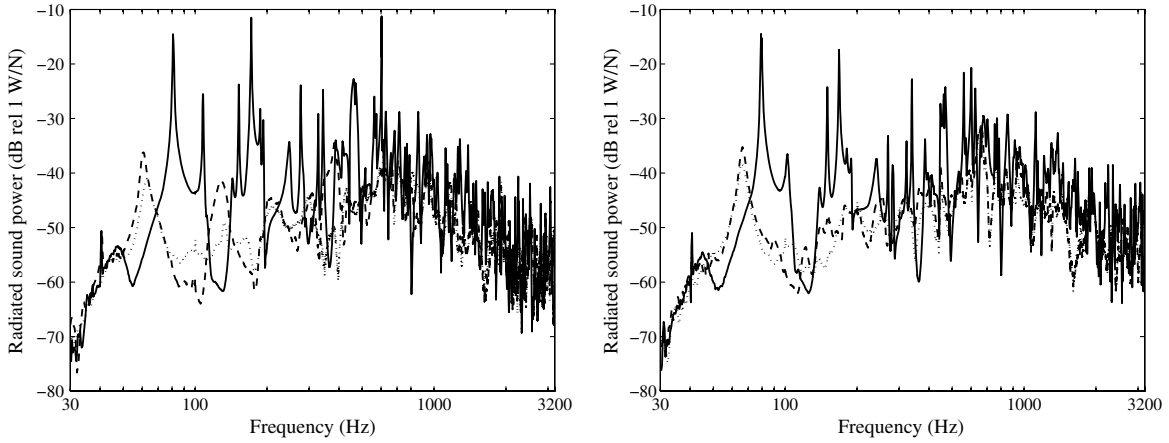

Fig. 12 Radiated sound power spectra for the configuration with honeycomb radiating panel. Deep air cavity (left), shallow air cavity (right), without sensors and actuators (solid lines), with open-loop sensors and actuators (dashed lines), and closed-loop with sensors and actuators (dotted lines).

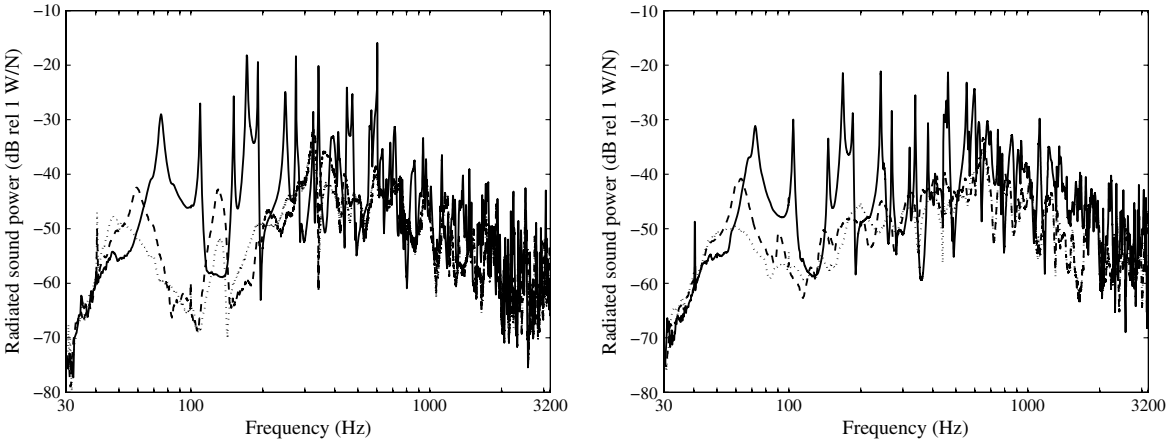

Fig. 13 Radiated sound power spectra for the configuration with Perspex radiating panel. Deep air cavity (left); shallow air cavity (right), without sensors and actuators (solid lines), with open-loop sensors and actuators (dashed lines), and with closed-loop sensors and actuators (dotted lines).

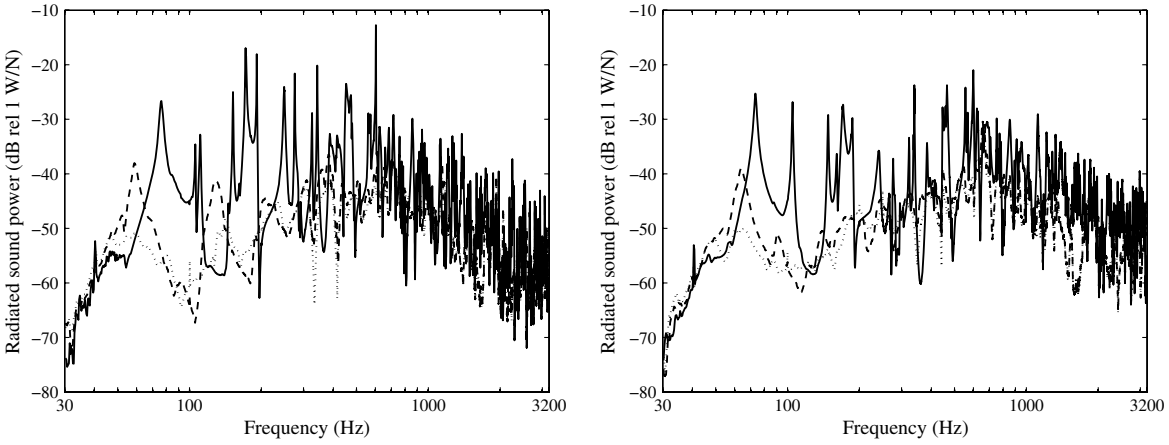

Fig. 14 Radiated sound power spectra for the configuration with aluminum radiating panel. Deep air cavity (left); shallow air cavity (right), without sensors and actuators (solid lines), with open-loop sensors and actuators (dashed lines), and with closed-loop sensors and actuators (dotted lines).

V. Conclusions

An active damping method using blended velocity feedback for the reduction of sound transmission through a simplified aircraft double panel is considered. The system is composed by a 3×3 array of decentralized feedback control units. Each unit is composed by an electrodynamic actuator reacting between the two panels and velocity sensors at the points where the actuator is connected with the source and radiating panels. The outputs of the source and radiating panel velocity sensors are weighted by factors α and $1-\alpha$, respectively. The two weighted outputs are subtracted and combined into the error signal. Stability and performance of the 3×3 system of velocity feedback loops is considered as a function of the velocity weighting factor used.

Metrics of the feedback-loop stability, which is the inverse of the maximum stable feedback gain δ_0 in this case, strongly depend on the velocity weighting factor used. In fact, there is a critical value of

the velocity weighting factor. For subcritical values of the velocity weighting factor, the open-loop sensor-actuator frequency response functions exhibit low-frequency phase lags, which compromise the stability, and decrease the available gain margin. However, if velocity weighting factors larger than the critical one are used, the low-frequency phase lags vanish and the available gain margin increases. Still, the maximum stable feedback gain is limited due to the sensor fundamental resonance, which causes high-frequency phase lags and, therefore, negative real parts of the open-loop sensor-actuator frequency response function.

By varying the velocity weighting factor between 0 and 1 it is possible to improve the performance of the active control system. In particular, the low-frequency sound radiation decreased with the increase of the velocity weighting factor. Consequently, large reductions of the radiated sound power were recorded at the lowest resonance of the smart double panel, varying between -12 and -18 dB, depending on the case studied. When the sound radiation of the double panel with no transducers mounted was compared with the sound radiation of the double panel with transducers, large passive mass and damping effects were observed in the broad frequency band.

Acknowledgments

The research work performed by Neven Alujević was supported by a Marie Curie Early Stage Training fellowship, within the research and training network "European Doctorate in Sound and Vibration Studies." Financial support was also provided to Neven Alujević by the Ministry of Science, Education, and Sport of the Republic of Croatia and Faculty of Mechanical Engineering and Naval Architecture of University of Split.

References

[1] Mixson, J. S., and Wilby, J. S., "Interior Noise," *Aeroacoustics of Flight Vehicles, Theory and Practice*, edited by H. H. Hubbard, NASA Langley Research Center, Hampton VA, 1995, pp. 271–335, Chap. 16.

[2] Wilby, J. F., "Aircraft Interior Noise," *Journal of Sound and Vibration*, Vol. 190, No. 3, 1996, pp. 545–564. doi:10.1006/jsvi.1996.0078

[3] Gardonio, P., "Review of Active Techniques for Aerospace Vibroacoustic Control," *Journal of Aircraft*, Vol. 39, No. 2, 2002, pp. 206–214. doi:10.2514/2.2934

[4] Fahy, F. J., and Gardonio, P., "Transmission of Sound Through Partitions," *Sound and Structural Vibration*, 2nd ed., Elsevier, London, 2007, pp. 277–374.

[5] Gardonio, P., and Elliott, S. J., "Active Control of Structure-Borne and Airborne Sound Transmission Through Double Panel," *Journal of Aircraft*, Vol. 36, No. 6, 1999, pp. 1023–1032. doi:10.2514/2.2544

[6] Elliott, S. J., Gardonio, P., Sors, T. C., and Brennan, M. J., "Active Vibroacoustic Control with Multiple Local Feedback Loops," *Journal of the Acoustical Society of America*, Vol. 111, No. 2, 2002, pp. 908–915. doi:10.1121/1.1433810

[7] Gardonio, P., Bianchi, E., and Elliott, S. J., "Smart Panel with Multiple Decentralised Units for the Control of Sound Transmission, Part 1: Theoretical Predictions," *Journal of Sound and Vibration*, Vol. 274, Nos. 1–2, 2004, pp. 163–192. doi:10.1016/j.jsv.2003.05.004

[8] Gardonio, P., Bianchi, E., and Elliott, S. J., "Smart Panel with Multiple Decentralised Units for the Control of Sound Transmission, Part 2: Design of the Decentralised Control Units," *Journal of Sound and Vibration*, Vol. 274, Nos. 1–2, 2004, pp. 193–213. doi:10.1016/j.jsv.2003.05.007

[9] Bianchi, E., Gardonio, P., and Elliott, S. J., "Smart Panel with Multiple Decentralised Units for the Control of Sound Transmission, Part 3: Control System Implementation," *Journal of Sound and Vibration*, Vol. 274, Nos. 1–2, 2004, pp. 215–232. doi:10.1016/j.jsv.2003.05.006

[10] Gardonio, P., "Sensor-Actuator Transducers for Smart Panels," *Proceedings of Active 2006*, Australia Acoustical Society, Adelaide, Australia, 18–20 Sept. 2006. pp. 1–12.

[11] Balas, M. J., "Direct Velocity Control of Large Space Structures," *Journal of Guidance and Control*, Vol. 2, No. 3, 1979, pp. 252–253. doi:10.2514/3.55869

[12] Sun, J. Q., "Some Observations on Physical Duality and Collocation of Structural Control Sensors and Actuators," *Journal of Sound and Vibration*, Vol. 194, No. 5, 1996, pp. 765–770. doi:10.1006/jsvi.1996.0394

[13] Jayachandran, V., and Sun, J. Q., "Unconditional Stability Domains of Structural Control Systems Using Dual Actuator-Sensor Pairs," *Journal of Sound and Vibration*, Vol. 208, No. 1, 1997, pp. 159–166. doi:10.1006/jsvi.1997.1177

[14] Alujević, N., Gardonio, P., and Frampton, K. D., "Smart Double Panel with Decentralized Active Damping Units for Sound Transmission Control," *AIAA Journal*, Vol. 46, No. 6, 2008, pp. 1463–1475. doi:10.2514/1.32369

[15] Alujević, N., Frampton, K. D., and Gardonio, P., "Stability and Performance of a Smart Double Panel with Decentralized Active Dampers," *AIAA Journal*, Vol. 46, No. 7, 2008, 1747–1756. doi:10.2514/1.34572

[16] Alujević, N., "Smart Double Panel with Decentralised Active Damping Units for the Control of Sound Transmission," Ph.D. Thesis, Univ. of Southampton, Institute of Sound and Vibration Research, Southampton, England, U.K., 2008, http://eprints.soton.ac.uk/64537/ [retrieved 17 Jan. 2011]

[17] Alujević, N., Gardonio, P., and Frampton, K. D., "Smart Double Panel with Decentralized Feedback Control Units for Blended Velocity Feedback," 2009 International Symposium on Active Control of Sound and Vibration, Ottawa, Canada, Paper ac09_365, 20–22 Aug. 2009.

[18] Elliott, S. J., "Multichannel Feedback Controllers," *Signal Processing for Active Control*, Academic Press, London, 2000, pp. 306–309.

N. Wereley
Associate Editor